Intersecting multiaxial domain walls in plastic ferroelectric crystal films

Yohei Uemura [1,*] Satoshi Matsuoka [1,2] Shunto Arai [1,†] Jun Harada [3] and Tatsuo Hasegawa [1]
[1]Department of Applied Physics, The University of Tokyo, Tokyo 113-8656, Japan
[2]Graduate School of Engineering, Nagasaki University, Nagasaki 852-8521, Japan
[3]Department of Chemistry, Hokkaido University, Sapporo 060-0810, Japan

(Received 11 September 2022; revised 12 December 2022; accepted 24 January 2023; published 2 March 2023)

Plastic ferroelectrics comprise a class of solution-processable molecular ferroelectrics, in which spherical polar molecules can rotate and/or freeze within crystal lattices. Some compounds exhibit superior multiaxial ferroelectricity and very sharp ferroelectric switching characteristics, although the domain wall (DW) characteristics have not yet been explored. Here, we report distinctive DW characteristics in drop-casted monocrystalline thin films of a typical plastic/ferroelectric [AH][ReO_4]. We demonstrate that the films form 71°, 109°, and 180° DWs, unique to the pseudocubic rhombohedral lattice, that emerge and compete with each other, depending on the crystallographic orientation of the films. Particularly, it is observed that all three types of DWs intersect at several single points, whose unique nature should be ascribed to the small elastic deformation. The observed domains and 180° DWs also comprise much larger periodicity and scaling than those of conventional inorganic ferroelectric films, which should be associated with the unique polarization reversal mechanism in the compound films. These observed features reveal the exotic multiaxial ferroelectricity of soft plastic/ferroelectrics, paving the way for developing printable ferroelectronics.

DOI: 10.1103/PhysRevMaterials.7.035601

I. INTRODUCTION

The emergence of ferroelectricity in molecular ferroelectrics is primarily based on spontaneous molecular transformations and/or displacements in weakly bonded molecular crystal lattices. The feature contrasts with that of inorganic ferroelectrics, which ordinally derive from collective ion displacements in rigid ionic crystal lattices, accompanied by notable lattice deformations [1–5]. It has been shown in the past decade that elaborate designs of component molecules allow us to develop several superior molecular ferroelectrics showing very large spontaneous polarizations and small coercive fields, as comparable with those of prominent inorganic ferroelectrics [6–12].

Plastic/ferroelectric crystals are a unique class of molecular ferroelectrics, taking advantage of the nature of plastic crystals: The plastic crystals are composed of spherical molecules that can rotate above the plastic transition temperature, while their positions are fixed, and whose rotation motions freeze below the transition temperature [13,14]. It was recently found that several plastic cocrystals, composed of polar cationic molecules and (nonpolar) anionic molecules, exhibit multiaxial ferroelectricity at room temperature [15–21]. A prominent example is 1-azabicyclo[2.2.1]heptanium perrhenate ([AH][ReO_4]), shown in Fig. 1(a) [21]. The compound forms a highly symmetric cubic lattice in the high-temperature paraelectric phase where the rotation motions of molecules suppress the emergence of ferroelectricity. In contrast, the spontaneous polarizations appear in the low-temperature phase (<322 K) owing to the orientational order of the polar cations whose rotation motions are frozen [Fig. 1(b)]. The achieved spontaneous polarization is coupled with a slight lattice deformation into a pseudocubic rhombohedral lattice. Eventually, multiaxial ferroelectricity is realized, which was not obtainable in other types of molecular ferroelectrics composed of molecules with lower symmetry.

Such multiaxial ferroelectricity allows us to obtain ferroelectric films that have a spontaneous polarization component normal to the film plane. The feature should form an ideal class of molecular materials toward thin-film device applications, coupled with the solution processability at ambient conditions. It was demonstrated that simple drop-casted thin films of [AH][ReO_4] exhibit low-voltage (<5 V) switching of large spontaneous polarization (7.8 $\mu C/cm^2$) at room temperature [21]. A particular feature is that very sharp ferroelectric switching characteristics are observed even with pellets of [AH][ReO_4] polycrystals. However, the unique nature of ferroelectric domain and domain wall (DW) characteristics remains to be explored in plastic/ferroelectric crystals [22,23]. These features are particularly important in understanding the origin of sharp switching characteristics as well as in disclosing the exotic multiaxial ferroelectricity coupled with weakly bonded rotatable molecules.

Here, we investigated ferroelectric domains and DWs in [AH][ReO_4] monocrystalline thin films produced via a drop-casting technique. We first categorize the obtained films in terms of crystallographic orientations. We then visualized the ferroelectric domains and DWs of the films, using three different types of techniques: crossed Nicols, birefringent ferroelectric field-modulation imaging (FFMI) [24],

*uemura@hsgw.t.u-tokyo.ac.jp
†Present address: Research Center for Functional Materials, National Institute for Materials Science (NIMS), Tsukuba, Ibaraki 305-0044, Japan.

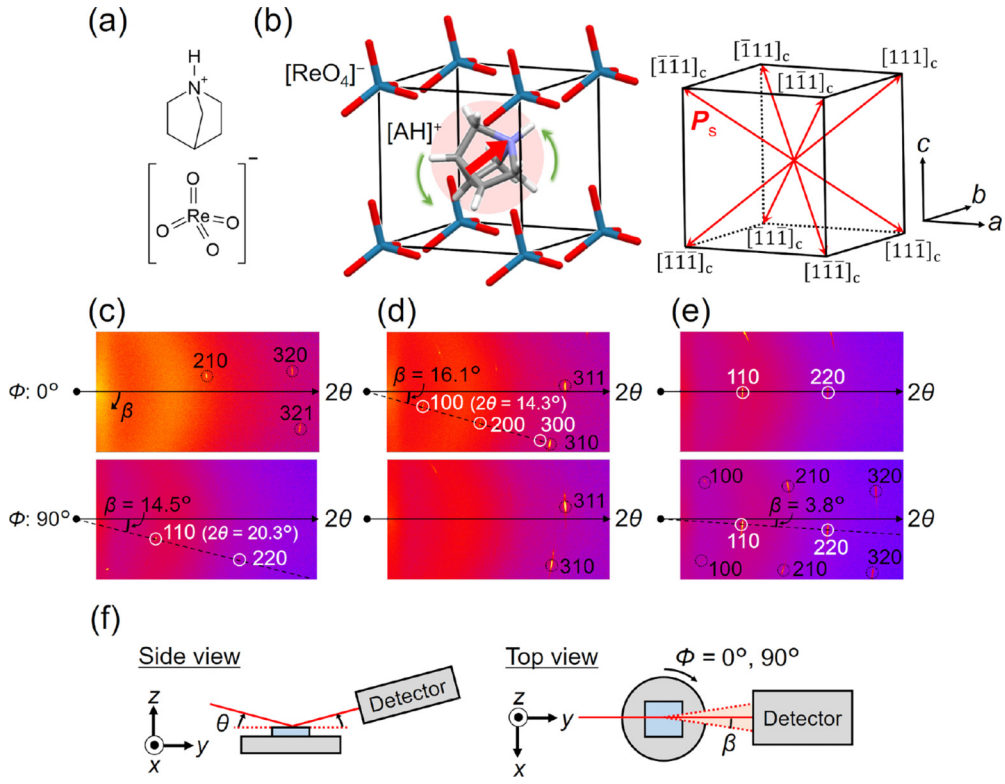

FIG. 1. Crystallographic orientation of $[AH][ReO_4]$ monocrystal films. (a) Molecular structures of AH^+ (top) and ReO_4^- (bottom). (b) Crystal structure of $[AH][ReO_4]$ (left) and its eight possible spontaneous polarization directions (right). We label the axes and plane indices with suffix c to denote the pseudocubic symmetry. Out-of-plane x-ray diffraction (XRD) images of $[AH][ReO_4]$ thin films: (c) type-A, (d) type-B, and (e) type-C films. XRD images are shown as functions of θ, Φ, and β, where θ is the incident angle of x rays, Φ is the in-plane angle of the sample, and β is the in-plane diffraction angle, as schematically shown in (f). The top images in (c)–(e) show the results for $\Phi = 0^\circ$, and the bottom images show the results for $\Phi = 90^\circ$. The central horizontal dashed lines correspond to $\beta = 0$. The measured range of the out-of-plane angle 2θ is $5-60^\circ$.

and piezoresponse force microscopy (PFM) [25,26]. We demonstrate that a combination of techniques allows us to analyze the overview and detailed view of the ferroelectric DW structures. Based on the observations and analyses, we discuss the unique nature of ferroelectric domains and DWs in terms of very small elastic deformations and polarization reversal mechanisms in the plastic/ferroelectric crystals.

II. EXPERIMENT

A. Thin-film fabrication and characterization

Thin films of $[AH][ReO_4]$ were obtained via a simple drop-casting technique. We used glass substrates (Matsunami Glass Ind., Ltd.) without surface treatments. We first fabricated striped bottom electrodes of Au (30 nm thickness)/Cr (2 nm) by vacuum evaporation. Thin films of $[AH][ReO_4]$ were then produced by casting an aqueous solution (4.0 wt. %) droplet on the substrate. The growth temperature was set at 343 K which is slightly higher than the ferroelectric-to-paraelectric transition temperature (322 K) [21]. The films were then slowly cooled to room temperature. The obtained films are polycrystalline composed of monocrystal-like grains with a typical lateral size of several hundred micrometers. We here use the term of *monocrystal* as a uniform and continuous microcrystal that has a specific pseudocubic crystallographic axis but is composed of several ferroelectric domains at the ferroelectric phase, formed during the cooling process across the transition temperature. A single monocrystal film was obtained by removing the other films with different crystallographic axis.

X-ray diffraction (XRD) measurements were conducted using a thin-film x-ray diffractometer (SmartLab, Rigaku) with a two-dimensional (2D) detector (HyPix-3000; Rigaku). The out-of-plane diffractions were measured along the two different in-plane axes (Φ) that were orthogonal to each other, as shown in Fig. 1(f). The crystallographic orientation was then determined from the observed diffraction spots of the respective films. The analysis was conducted assuming that the crystal is pseudocubic. A series of diffractions were observed with a deviation angle β from the midline of the 2D detector, which was associated with the inclination of the lattice plane from the substrate plane. The crystallographic orientations of the respective films were analyzed based on the 2θ and β values of the observed diffraction spots.

B. Crossed Nicols and birefringent FFMI measurements

Both crossed Nicols and birefringent FFMI measurements were conducted with polarized optical microscopy. The latter is to detect slight changes in polarized optical microscope image caused by application of alternating electric fields in

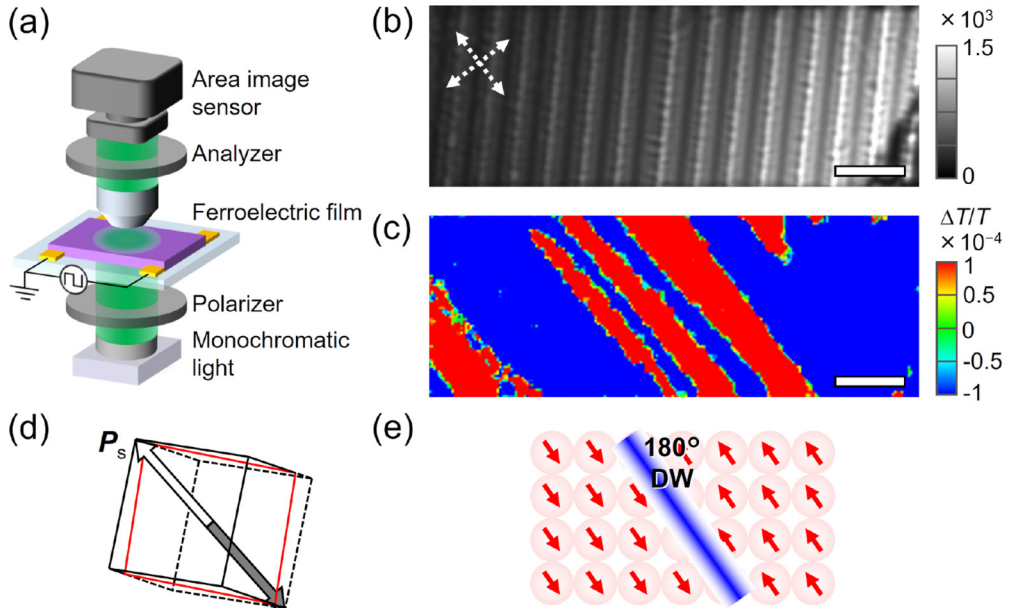

FIG. 2. Birefringent ferroelectric field-modulation imaging (FFMI) measurement of $[AH][ReO_4]$ thin films. (a) Schematic of the optical setup. (b) Crossed Nicols micrograph and (c) birefringent FFMI image of the film. The two white-dotted arrows in (b) (being orthogonal to each other) indicate the extinction directions as observed in the crossed Nicols micrograph. (d) Pseudocubic unit cell of a type-A film, viewed along a normal to the substrate plane. The red frame represents the plane parallel to the substrate plane. The in-plane crystallographic orientation is same as the orientation of the film shown in (b) and (c). The white and gray arrows indicate the orientations of spontaneous polarizations, as observed in (c). (e) Schematic of the possible spontaneous polarization directions around the 180° domain walls (DWs). Scale bar is 20 μm.

the films [24]. The difference of the measurements is that it is not possible to detect 180° DWs by crossed Nicols but becomes possible by birefringent FFMI. The combination of the measurements allows us to obtain whole features of ferroelectric domains and DWs over a wide area (more than several hundred squared micrometers) of the films within short time. The measurements also allow us to detect the features of DWs along the depth direction.

A setup for birefringent FFMI is schematically depicted in Fig. 2(a). A change in optical birefringence induced by external in-plane electric fields causes a change in transmitted light intensity, which is sensitively detected by a modulation technique with use of an area-image sensor. We used a home-built setup composed of a polarizing microscope and a complementary metal oxide semiconductor (CMOS) area image sensor (pco.edge 5.5; PCO AG). An LED (M660L4; THORLABS) was used as the light source, and a pair of linear polarizers was inserted in the front and back of the sample film. A square-wave bias voltage was applied between a pair of striped electrodes at a frequency f during the measurements. Optical images were captured by the CMOS sensor at a frequency of $2f$, synchronized with the bias voltage to acquire images at the positive and negative bias states. The spatial distribution of the transmittance modulation ($\Delta T/T$) was visualized by calculating the difference (ΔT) and average (T) of the positive- and negative-bias images, respectively, at each pixel. The obtained $\Delta T/T$ images were integrated $2^{14}(= 16\,384)$ times to reduce noise. The frequency f used in this study was 10–20 Hz, and the amplitude of the modulation voltage was $10\,V_{p-p}$. The applied electric fields were estimated as 0.2 kV/cm, which is lower than the coercive field of $[AH][ReO_4]$ [21].

C. PFM measurements

PFM allows us to obtain more detailed information on the three-dimensional (3D) directions of spontaneous polarizations within narrow areas at the film surfaces. PFM measurements were conducted with a commercially available scanning probe microscope (MFP-3D, Oxford Instruments) using a conducting tip (PPP-NCSTPt-20; Nanosensors). To analyze the 3D direction of spontaneous polarizations, the out-of-plane component (z) and two in-plane components (x, y) were measured using vertical- and lateral-mode PFMs, respectively. The x and y components were individually measured with different in-plane angles that were orthogonal to each other. All the measurements were conducted on $[AH][ReO_4]$ films without top electrodes under ambient conditions.

Note that PFM can only determine the relative relationship between the spontaneous polarizations of adjacent domains, whereas birefringent FFMI allows determining the spontaneous polarization direction by examining the change of polarization directions with applied electric fields.

III. RESULTS AND DISCUSSIONS

A. Crystallographic orientation of thin films

The crystallographic orientations of the monocrystal-like films were investigated using out-of-plane XRD. The observed diffraction spots exhibit arclike spreads, as presented in Figs. 1(c)–1(e), the feature of which is ascribable to the slight distribution of crystallographic orientations of the films.

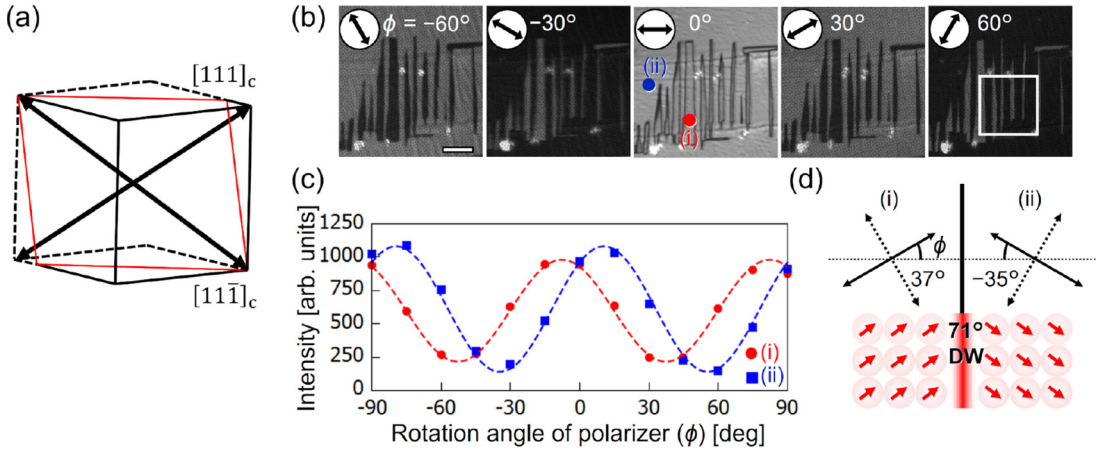

FIG. 3. Incident polarizer angle-dependent crossed Nicols microscopy image of a type-A [AH][ReO_4] thin film. (a) Pseudocubic unit cell of a type-A film, viewed along a normal to the substrate plane. The red frame represents the plane parallel to the film (or substrate) plane. (b) Crossed Nicols micrographs of a type-A monocrystal-like film with varying incident light polarization angle (black arrows). The in-plane crystallographic orientation of the film is set to be coincident with (a). The white square shown in the rightmost image represents the area where the piezoresponse force microscopy (PFM) analysis, shown in Fig. 4, was conducted. (c) Dependence of the transmitted light intensity on the polarization angle of the incident light. The red-filled circles and blue-filled squares represent the results obtained at the two different regions denoted as (i) and (ii) in the middle image of (b), respectively. The dashed curves show the fitting of the experimental results using Eq. (1). (d) Schematics for the extinction direction in regions (i) and (ii) (top) and for the possible spontaneous polarization directions around the 71° domain walls (DWs; bottom). The solid black arrows are consistent with the polarization axes shown in (a), while the dashed arrows are not consistent with any $\langle 111_c \rangle$ axes. Scale bar in (b) is 10 μm.

We analyzed the diffractions observed at $\Phi = 0^\circ$ and 90° by assuming the pseudocubic crystal symmetry and roughly determined the orientations of the crystallographic axes of the films.

From the results for several samples, we found that the films grown on flat glass substrates have surfaces that do not correspond to simple or primary crystallographic plane. The crystallographic orientation of the films can be categorized into at least three types: type A is the film in which the $\{110\}_c$ plane is inclined at ∼15° to the substrate surface; type B, in which the pseudocubic $\{100\}_c$ plane is inclined at 15–20° to the substrate surface; and type C, wherein the $\{110\}_c$ plane is almost parallel to the substrate surface. Of the six measured samples, two were type A, three were type B, and one was type C (all measured data are presented in Supplemental Material Figs. S1–S3 [27]). The thickness of the films is ranged between 1.1 and 5.2 μm. These results indicate that the nonepitaxial crystalline films of [AH][ReO_4] tend to grow along a few crystallographic orientations on glass substrates.

B. Crossed Nicols observation of 71° DWs

We first show an example of crossed Nicols microscope observations for a type-A film in Fig. 3. Figure 3(a) depicts the directional relationship between the pseudocubic unit cell and the substrate plane, viewed from the normal to the substrate plane whose crystallographic direction is shown by the red frame. Figure 3(b) displays a series of micrographs taken at various polarizer angles, where the images are arranged so that the in-plane orientation of the film coincides with that of the red frame shown in Fig. 3(a). It is seen that each image contains several clear bright-to-dark boundaries where the brightness of the adjacent region changes, simultaneously, depending on the polarizer angle. The observation clearly indicates that the boundaries should correspond to DWs except 180° DWs. (The crossed Nicols cannot visualize the 180° DWs, as adjacent spontaneous polarizations are antiparallel to each other.) Figure 3(c) presents the dependence of the transmitted light intensity (I) on the incident polarization angle (ϕ), measured at each region, as denoted by (i) and (ii) in the middle image of Fig. 3(b). The dependence of I on ϕ is well fitted by the following equation:

$$I = I_0 \sin^2(\phi - \phi_0) + c, \quad (1)$$

where I_0, ϕ_0, and c are the fitting parameters. Here, we define $\phi = 0^\circ$ as the angle at which the incident polarization is roughly orthogonal to the long DW lines, as observed in the crossed Nicols image in Fig. 3(b). The fitting results indicate that $\phi_0 = +37^\circ$ or -53° in region (i) and $\phi_0 = -35^\circ$ or $+55^\circ$ in region (ii), as illustrated in Fig. 3(d). By comparing with the crystallographic $\langle 111 \rangle_c$ axes of the film shown in Fig. 3(a), it is most probable that the spontaneous polarization (i.e., $[111]_c$) should be directed at $\phi = +37^\circ$ in regions (i) and at $\phi = -35^\circ$ in regions (ii), respectively. Thus, we consider that the boundaries of the bright-to-dark contrast in Fig. 3(b) should be attributed as the 71° DWs. It is important to point out that this presumption is confirmed by the PFM analysis on the same region of the film, as discussed later (Fig. 4).

As a complement to the observations, we evaluated the optical birefringence of [AH][ReO_4] via polarized transmittance spectra with use of polarizer and analyzer (Supplemental Material S2 and Fig. S4 [27]). We found that the [AH][ReO_4] film exhibits a very small birefringence (∼0.01). The result demonstrates the highly optically isotropic nature of [AH][ReO_4], providing a consistent picture on the

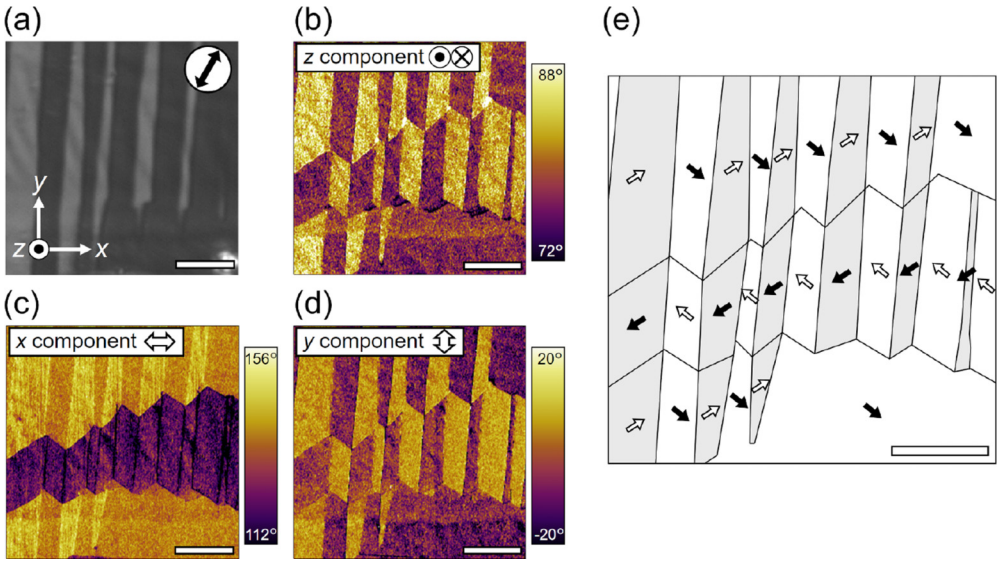

FIG. 4. Three-dimensional (3D) piezoresponse force microscopy (PFM) analysis of a type-A thin film of [AH][ReO_4]. (a) Crossed Nicols micrograph of the measured area. PFM phase images measured along (b) z, (c) x, and (d) y components for the spontaneous polarization. (e) Schematic representation of the analyzed domain structure. The white- and gray-colored regions represent the different axes of spontaneous polarization. The direction of the arrows indicates the in-plane orientation of spontaneous polarization, while the white and black arrows indicate the up and down orientations of the out-of-plane components, respectively. Scale bar is 5 μm.

considerably small deviation of the rhombohedral lattice from the cubic lattice ($\alpha = 89.85^\circ$), although the films exhibit very large spontaneous polarization (7.8 $\mu C/cm^2$) [21].

C. Visualization of 180° and multiaxial DWs using birefringent FFMI

Here, we demonstrate that the combined measurements of conventional crossed Nicols and birefringent FFMI [Fig. 2(a)] can visualize 180° DWs and determine the polarization direction in each domain. Figure 2 shows an example of the birefringent FFMI conducted for a type-A film. The thickness of the film is 5.2 μm. Here, we chose a specific area of the film that presents uniform optical anisotropy but a notable bright-to-dark contrast in the crossed Nicols image owing to the wavy undulation in thickness distribution, as shown in Fig. 2(b) and Supplemental Material Fig. S5 [27]. The feature indicates that the area does not involve DWs except 180° DWs. Here, we note that most of the [AH][ReO_4] films are not smooth but have corrugated surfaces, as presented in Supplemental Material Fig. S6 [27]. Nonetheless, the tilting angle of respective flat regions from the horizontal plane is estimated to be as small as 9° at the largest (ranged between 3° and 9°) from the AFM profiles of the films. Figure 2(c) presents the results of the birefringent FFMI measurements. Clearly striped domain structures are observed as the contrast of positive and negative transmittance modulation ($\Delta T/T$) signals, as indicated by the red and blue regions, respectively. The boundaries between the blue and red stripes should be attributed as the 180° DWs. Note that such a periodic alignment of 180° DWs is frequently observed in the films. Comparing with the crystallographic $\langle 111 \rangle_c$ axes, it is most probable that the spontaneous polarization direction should correspond to the arrows in Fig. 2(d), which is roughly parallel to the observed DWs. It indicates that the observed 180° DWs should be neutral domains, as schematically depicted in Fig. 2(e). The periodic alignment should be associated with the suppression of depolarization fields caused by the out-of-plane component of spontaneous polarization within the films [28,29], as discussed later.

We also conducted birefringent FFMI observations for another area, involving DWs except 180° DWs, the result of which is shown in Fig. 5. The thickness of the film is 3.0 μm. The crossed Nicols micrograph of the area, shown in Fig. 5(a), exhibits clear boundaries of bright-to-dark contrast, which can be ascribed to the DWs except 180° DWs. Notably, the birefringent FFMI image of the area, shown in Fig. 5(b), presents a slightly complicated blue-to-red contrast. To analyze the detailed DW structure, a comparison is made between the crossed Nicols and FFMI images; Fig. 5(c) shows an overlay of the images. We found that the boundaries as observed in the images can be distinctly classified into the following three cases: boundaries where both crossed Nicols and FFMI images show clear contrast (shown by red lines), boundaries where crossed Nicols shows contrast while FFMI does not (shown by green lines), and boundaries where crossed Nicols does not show contrast while FFMI does (shown by blue lines). Though the XRD measurement was not conducted for the film, it is clear that red and green lines could be ascribed to either 71° or 109° DWs or vice versa, whereas the blue lines are ascribed to 180° DWs, based on similar arguments for Figs. 2 and 3. The results demonstrate that the 71°, 109°, and 180° DWs coexist in the [AH][ReO_4] films. We also noticed several unique spots where three different types of DWs intersect at a single point, as depicted by circles in Fig. 5(c). The observation is quite unique, in contrast to the observations for inorganic ferroelectrics in which the domain structures are only

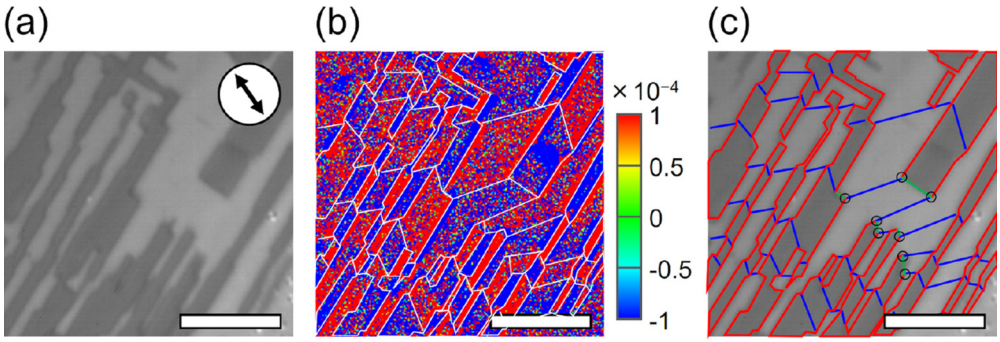

FIG. 5. Birefringent ferroelectric field-modulation imaging (FFMI) measurement of multiaxial domains. (a) Crossed Nicols micrographs and (b) the corresponding birefringent FFMI image. Domain boundaries identified via the crossed Nicols micrographs and birefringent FFMI are shown by white lines in (b). (c) Overlay of the images in (a) and boundaries in (b). Domain boundaries as observed in (a) and (b) are classified into the three cases; boundaries shown by red lines where contrast is observed in both (a) and (b), boundaries shown by green lines where contrast is observed in (a) but not in (b), and boundaries shown by blue lines where contrast is observed in (b) but not in (a). Black circles indicate the unique spots where three types of domain walls (DWs) intersect. Scale bar is 10 μm.

composed of a pair of 71° and 180° DWs (or a pair of 109° and 180° DWs).

We also notice that the birefringent FFMI signal intensity is considerably enhanced around the 71° DWs. We found that the signal enhancement can be ascribed to the tilt of the DWs from a normal-to-the-substrate plane, as described in detail in the Supplemental Material S5 and Fig. S7 [27]. We found that the birefringent FFMI signal is enhanced either positively or negatively as a function of the distance from the boundary line, when the DWs are tilted from the normal of the substrate plane (Supplemental Material Figs. S7(a)–S7(c) [27]). The feature is consistent with the observation of the thick dark lines at both 71° and 109° DWs in the crossed Nicols image, as observed in the middle image of Fig. 3(b) and Supplemental Material Fig. S7(d) [27]. Therefore, the thick dark lines in the crossed Nicols image and the notable enhancement of the FFMI signal is a clear sign of the inclination of the DW structures within the films.

D. PFM observation and analysis

We conducted 3D PFM analysis to investigate the unique domain structures as observed in crossed Nicols and birefringent FFMI images. Out-of-plane and in-plane PFM measurements were conducted to analyze the 3D orientations of spontaneous polarizations in the respective domains of the [AH][ReO_4] thin films. The analysis was performed for each type-A, B, and C film to reveal the relationship between the domain structure and crystallographic orientation. A crossed Nicols micrograph is shown in Fig. 4(a) for a type-A film, in which the detailed PFM analyses were conducted. The thickness of the film is 2.8 μm. We defined the orthogonal x, y, and z axes, as shown in the figure. In the 3D PFM analyses, we determined the z component through out-of-plane piezoresponse force measurements, while the x and y components via independent in-plane piezoresponse force measurements.

The PFM phase images measured along the z, x, and y components are shown in Figs. 4(b)–4(d), respectively. The 180° DWs that are not observed in the crossed Nicols image are clearly seen in the PFM image. All the PFM images allow us to analyze the 3D spontaneous polarization orientations of the respective ferroelectric domains, the result of which is presented in Fig. 4(e). The in-plane angle of the spontaneous polarization was determined from the extinction directions of crossed Nicols observation, as shown in Fig. 4(a). Here, we note that all the polarization orientations, as presented in Fig. 4(e), can be reversed because the relative relationship of polarization orientation between the adjacent domains can be analyzed in the PFM phase image. We found from Fig. 4(e) that only two different axes, out of four possible $\langle 111\rangle_c$ axes in the pseudocubic unit cell, form the spontaneous polarization orientations in the film.

From the PFM analyses and the comparison with XRD measurements, we classified the observed DWs into 71°, 109°, and 180° DWs, the result of which is presented in Fig. 6(a). Here, the 71°, 109°, and 180° DWs are depicted by red, green, and blue lines, respectively. Figures 6(b)–6(d) show the relation between these DWs and the crystallographic orientations, where the in-plane orientation of crystal lattice in Figs. 6(b)–6(d) is set to be coincident with that in Fig. 6(a). The combination of polarization orientations at each DWs are found to be $[111]_c$ and $[11\bar{1}]_c$ at 71° DWs, $[111]_c$ and $[\bar{1}\bar{1}1]_c$ at 109° DWs, and $[111]_c$ and $[\bar{1}\bar{1}\bar{1}]_c$ at 180° DWs. The white (black) arrows in Figs. 6(b)–6(d) indicate that the orientations of the out-of-plane components are upward (downward) against the substrate plane, as is consistent with the result of out-of-plane PFM. The result in Fig. 6(a) shows that all the 71°, 109°, and 180° DWs are contained in the image, which is consistent with the result of the birefringent FFMI image shown in Fig. 5(b). Additionally, we found that the domain structure is dominantly composed of 71° and 180° DWs, while only a few 109° DWs exist, which were commonly observed in the type-A films.

The crossed Nicols micrographs and PFM images for the type-B and C films are presented in Supplemental Material Figs. S8 and S9 [27]. In the type-C film, it was not possible to detect the out-of-plane component of spontaneous polarization, as it was too small. Thus, we determined the in-plane component by PFM and then assumed the out-of-plane component which is consistent with the crystallographic orientation measured by XRD. The results of the analyses

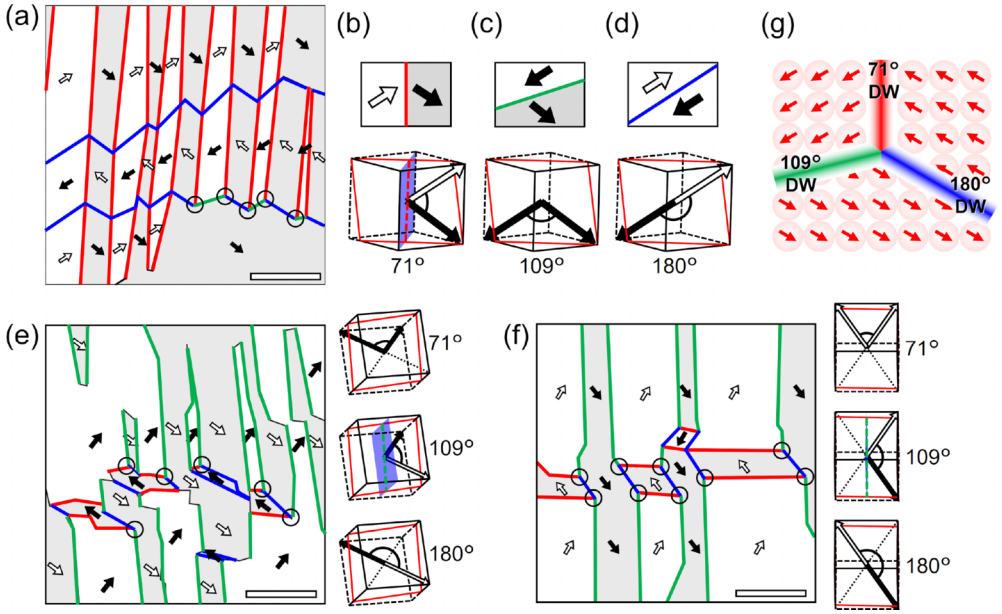

FIG. 6. Analysis of domain structure in type-A, B, and C thin films of $[AH][ReO_4]$. (a) Domain structure of type-A film [same as Fig. 4(e)]. The color of the domain walls (DWs) indicates the type of DW: red: 71° DW//$[110]_c$, green: 109° DW//$[100]_c$, and blue: 180° DW//P_s. The open circles denote the spots where the 71°, 109°, and 180° DWs join at a single point. Orientations of spontaneous polarization at (b) 71°, (c) 109°, and (d) 180° DWs in the type-A film. The respective bottom figures show schematic representations of the unit cell determined via x-ray diffraction (XRD) measurements, where the red frame represents the plane parallel to the substrate plane. The white and black arrows indicate positive and negative z components of the spontaneous polarizations, respectively. (e) Domain structures of type-B and (f) type-C films, analyzed from piezoresponse force microscopy (PFM) images (shown in Supplemental Material Figs. S8 and S9 [27], respectively). The red, green, and blue lines represent the 71°, 109°, and 180° DWs, respectively. The figures on the right present the crystallographic orientation and the direction of spontaneous polarization at each type of DW. (g) Schematics of the unique spots where the 71°, 109°, and 180° DWs join at a single point [shown by black circles in (a), (e), and (f)]. Scale bars are 5 μm.

for the type-B and C films are shown in Figs. 6(e) and 6(f), respectively. The thicknesses of the films are 1.1 and 1.6 μm, respectively. We found that most DWs are predominated by the 109° DWs in both types of films, which is in sharp contrast to the case of the type-A film.

E. On the population and intersection of multiaxial DWs

Let us first discuss the origin of why the observed domain structures were formed in the respective films. We point out that two different axes ($[111]_c$ and $[11\bar{1}]_c$) out of four $\langle 111\rangle_c$ axes preferentially form the spontaneous polarizations whose out-of-plane components are small, the features of which are observed for all the types (A, B, and C) of film, as presented in Fig. 6. We also notice that all the 71° and 109° DWs are composed of head-to-tail alignments of the adjacent spontaneous polarizations because this feature minimize the electrostatic energy. Based on these common features, we found, in the case of the type-A film, that the out-of-plane component is reversed at the 71° DWs but is maintained at the 109° DWs. Thus, charges on the film surface are canceled at the 71° DWs but not at the 109° DWs. It means that the 71° DWs should be more stable than the 109° DWs in terms of the out-of-plane depolarization field. This consideration is consistent with the observation that the 71° DWs are dominant, while only a few 109° DWs exist in the type-A film. In contrast, the out-of-plane component is reversed at the 109° DWs but is maintained at the 71° DWs in the type-B and C films. Thus, the features should lead to the observation that the number of the 109° DWs is larger than that of the 71° DWs. It should be noted here that the population difference between 71° and 109° DWs should be associated with the fact that the film plane is not parallel to but is slightly inclined from the primary crystallographic plane such as $\{110\}_c$.

Then we focus on the roles of lattice strains at the 71° and 109° DWs. As spontaneous polarizations are directed toward the longest diagonal line of the rhombohedron lattice in $[AH][ReO_4]$, the 71° and 109° DWs should be accompanied by slight lattice deformations. Here, we point out that the deviation angle from the cubic lattice is as small as 0.15° ($\alpha = 89.85°$) [21], which leads to a small but non-negligible elastic energy. The mechanical strain at the DWs can be minimized when the adjacent domains are deformed equivalently along certain crystallographic planes [28]. In fact, the orientation of the 71° DWs as observed in Fig. 6(a) is almost parallel to the $\{110\}_c$ plane [as denoted by the purple plane in Fig. 6(b)], while the 109° DWs are involved in the $\{100\}_c$ plane, as observed in Figs. 6(e) and 6(f). The arguments are consistent with the fact that most of the 71° and 109° DWs are linearly extended and aligned with each other within monocrystal-like domain films, as is frequently observed in many other ferroelectrics [28,29]. All the results indicate that the population of each type of DW is associated with the stability of DWs, as determined to minimize both out-of-plane depolarization field and lattice strains at the DWs.

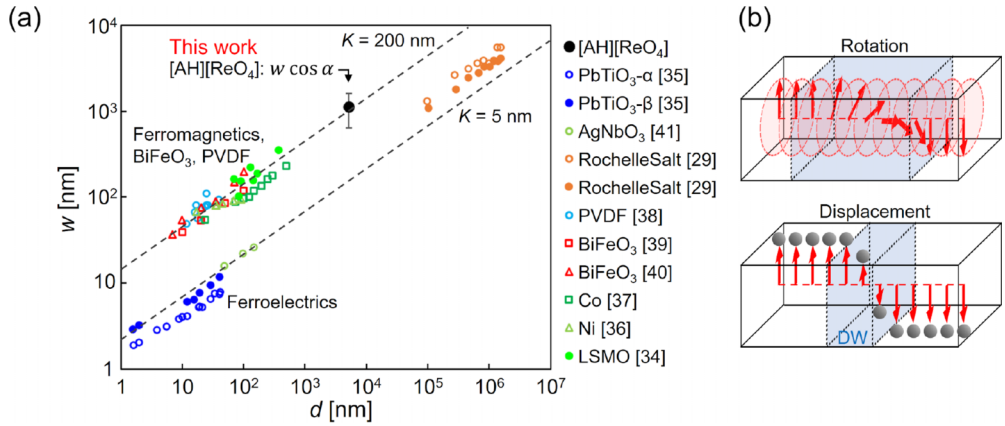

FIG. 7. (a) Relationship between the domain size and the film thickness. The domain size is plotted for various ferroic materials including ferromagnetics, multiferroics, polymer ferroelectrics, and [AH][ReO_4]. Data other than [AH][ReO_4] are quoted from references. The domain size of [AH][ReO_4] was modified using the tilting angle of spontaneous polarization from the normal to the film plane α as $w \cos\alpha$. The two dashed lines provide an eye guide for $K = 5$ and 200 nm, respectively. (b) Schematics of the domain wall (DW) structure, in which electric dipoles (red arrows) rotate without the change in magnitude (top) and ions displace along polarization axis (bottom).

By contrast, the 180° DWs should not involve lattice strains, as the longest diagonal lines are common to the adjacent domains. Instead, charge neutrality would be broken at the DWs, if they are not parallel to the spontaneous polarization. A unique feature is that the 180° DWs as observed in Fig. 6(a) frequently change the directions considerably when they are intersected with the 71° DWs, although the 71° DWs are slightly curved but extended straight over long distances. It is clear from the observations that the 180° DWs are more flexible against winding or bending. In this context, a more unique observation is that there exist several unique spots where the 71°, 109°, and 180° DWs intersect (or join) together in all the types of film, as denoted by the open circles in Figs. 6(a), 6(e), and 6(f). Such a multiaxial coexistence of the DWs is schematically depicted in Fig. 6(g). The features contrast with the DWs in inorganic ferroelectrics, where most DWs are composed of only a pair of 71° and 180° DWs (or 109° and 180° DWs) [28]. We consider that very small lattice deformation or mechanical softness, unique to the plastic/ferroelectric crystals, should allow the multiaxial coexistence of 71°, 109°, and 180° DWs.

F. On the periodicity and scaling of 180° DWs

We then discuss the periodicity of DWs or average domain width (w) in the plastic/ferroelectric films of [AH][ReO_4]. We find that w is very large of the order of a few micrometers, as compared with narrower w of the order of a few or several tens of nanometers in other ferroelectric materials [29,30]. Here, we consider Kittel's law for the domain-size scaling, represented as $w^2 = Kd$, where K is constant and d is the film thickness [31–33]. Figure 7(a) shows the relationship between w and d (Supplemental Material Fig. S5 [27]), obtained for various ferroic materials [29,34–41]. We plot the values for 180° DWs in the type-A films of [AH][ReO_4] (the thickness is 5.2 μm) because these DWs are unique and free from the effect of lattice strains, as discussed in the former subsection. For the proper comparison, here, we modified the domain width as $w \cos\alpha$ (α is the tilting angle of spontaneous polarization from the vertical direction to the plane, which is estimated as 82.4° in this case) because Kittel's law assumes the domain energy in terms of the depolarization fields normal to the plane. We found that the K value estimated from the plot for plastic/ferroelectric crystal films is ∼ 240 nm, which is deviated from the value for perovskite ferroelectrics ($K \approx 5$ nm) but comparable with that of ferromagnetics ($K \approx 200$ nm). Schilling *et al.* [31] discussed that the difference of the K values should be ascribed to the difference of DW width (δ), i.e., $K \propto \delta$. In this context, the DW width of [AH][ReO_4] is like that of ferromagnetics ($\delta \sim 20$ nm) rather than that of perovskite ferroelectrics ($\delta \sim 1$ nm).

In plastic/ferroelectric materials, rotation motion of spherical molecules is frozen in the ferroelectric state, in which the alignment of polar molecules is coupled with weak lattice distortion from the cubic lattice. As component spherical cationic molecules involve a permanent electric dipole, switching of spontaneous polarization at DWs should be accompanied by the collective rotation of molecules [Fig. 7(b), top]. The feature contrasts with the inorganic ferroelectrics such as perovskites, where the ferroelectric switching is accompanied by collective ion displacements [Fig. 7(b), bottom] and notable lattice deformations. Particularly, the case of 180° DWs in [AH][ReO_4] can be regarded as ideal because the interaction between spontaneous polarizations at the DWs should be dominated by pure dipole-dipole interactions between polar spherical molecules without lattice strains at the DWs. In such a case, the switch of the polarization reversal at the 180° DWs should be gradual, and the DW width can be very large which could be broadened by dipole-dipole interaction. We consider that the estimated large width of the DWs should be closely associated with the sharp switching behavior because the DWs with large widths should be weakly pinned by defects. In fact, [AH][ReO_4] are known to exhibit sharp switching of spontaneous polarization even in pressed polycrystals, showing rectangular *P-E* hysteresis loops like those of single crystals [15,21], which is in sharp contrast to the case of inorganic ferroelectrics. Further investigation of the nature of DWs should lead to an understanding of the unique characteristics

of plastic/ferroelectric materials, which are indispensable for ferroelectric applications.

IV. CONCLUSIONS

In this paper, we successfully reveal the unique characteristics of ferroelectric domains and DWs in plastic/ferroelectric thin films, depending on the crystallographic orientations. A simple drop-casting technique allowed the fabrication of polycrystalline films of [AH][ReO_4], involving large monocrystalline films with a large lateral size of several hundred squared micrometers. The obtained thin films were classified as comprising at least three types of crystallographic orientations. Moreover, we utilized three different techniques for overview and detailed view observations for the ferroelectric domains and DWs: crossed Nicols, birefringent FFMI, and PFM.

The investigations revealed the features of the ferroelectric domains and DW characteristics in [AH][ReO_4] thin films as follows: First, it was found that the domain structure comprised three types of DWs, 71°, 109°, and 180° DWs, unique to the pseudocubic ferroelectric crystals. The 71° and 109° DWs, which are accompanied by lattice deformation, were visualized through crossed Nicols micrographs, while the 180° DWs without lattice deformation were observed via the birefringent FFMI technique. We found that the emerging ratio of these three types of DW depends on the crystallographic orientation of the film, which originates from the fact that the domains and DWs form to cancel the electric charge on the film surfaces. In addition, DWs were formed in the orientation that the electrostatic energy and mechanical strain at DWs are minimized. The results indicate that the formation of DWs in [AH][ReO_4] should be dominated by the suppression of the depolarization field and the energy minimization for DW generation, the mechanism of which is usually known in perovskite ferroelectrics. On the other hand, peculiar phenomena unique to plastic/ferroelectric films were observed in the nature of the DWs. It was found that unique spots exist where the 71°, 109°, and 180° DWs stably coexist to intersect at a point. Moreover, the DW widths were estimated to be much wider than those of perovskite ferroelectrics, which can be ascribed to the gradual rotation of polar molecules around the DWs. These unique features have never been observed in perovskite ferroelectrics, whose spontaneous polarization is strongly coupled to lattice deformation.

The results presented above provide significant implications for the realization of ferroelectronics based on plastic/ferroelectric materials. We believe that the findings on peculiar DW characteristics should lead to further studies on DW engineering that may improve and develop ferroelectric properties such as piezoelectricity and pyroelectricity based on the functionality of DWs. The multiaxial ferroelectricity and solution processability, coupled with the unique nature of DW characteristics in plastic/ferroelectric materials, should lead to the realization of printable ferroelectronics devices.

ACKNOWLEDGMENTS

This paper was partially supported by JSPS KAKENHI (Grants No. JP19H02579, No. JP21H05234, No. JP22H01933, and No. JP18J22030), and JST CREST (Grant No. JPMJCR18J2).

[1] T. Mikolajick, U. Schroeder, and S. Slesazeck, The past, the present, and the future of ferroelectric memories, IEEE Trans. Electron. Devices **67**, 1434 (2020).

[2] M. H. Lee, R. Guo, and A. S. Bhalla, Pyroelectric sensors, J. Electroceram. **2**, 229 (1998).

[3] P. Muralt, Ferroelectric thin films for micro-sensors and actuators: A review, J. Micromech. Microeng. **10**, 136 (2000).

[4] H. Ishizuki and T. Taira, High-energy quasi-phase-matched optical parametric oscillation in a periodically poled MgO : $LiNbO_3$ device with a 5 mm × 5 mm aperture, Opt. Lett. **30**, 2918 (2005).

[5] D. Janner, D. Tulli, M. G. Granda, M. Belmonte, and V. Pruneri, Micro-structured integrated electro-optic LiNbO3 modulators, Laser Photonics Rev. **3**, 301 (2009).

[6] T. Akutagawa, H. Koshinaka, D. Sato, S. Takeda, S. Noro, H. Takahashi, R. Kumai, Y. Tokura, and T. Nakamura, Ferroelectricity and polarity control in solid-state flip-flop supramolecular rotators, Nat. Mater. **8**, 342 (2009).

[7] H. Okamoto, T. Mitani, Y. Tokura, S. Koshihara, T. Komatsu, Y. Iwasa, T. Koda, and G. Saito, Anomalous dielectric response in tetrathiafulvalene-p-chloranil as observed in temperature- and pressure-induced neutral-to-ionic phase transition, Phys. Rev. B **43**, 8224 (1991).

[8] S. Horiuchi, K. Kobayashi, R. Kumai, and S. Ishibashi, Ionic versus electronic ferroelectricity in donor–acceptor molecular sequences, Chem. Lett. **43**, 26 (2014).

[9] S. Horiuchi and S. Ishibashi, Hydrogen-bonded small-molecular crystals yielding strong ferroelectric and antiferroelectric polarizations, J. Phys. Soc. Jpn. **89**, 051009 (2020).

[10] S. Horiuchi, K. Kobayashi, R. Kumai, and S. Ishibashi, Proton tautomerism for strong polarization switching, Nat. Commun. **8**, 14426 (2017).

[11] K. J. Choi, M. Biegalski, Y. L. Li, A. Sharan, J. Schubert, R. Uecker, P. Reiche, Y. B. Chen, X. Q. Pan, V. Gopalan *et al.*, Enhancement of ferroelectricity in strained $BaTiO_3$ thin films, Science **306**, 1005 (2004).

[12] G. Catalan and J. F. Scott, Physics and applications of bismuth ferrite, Adv. Mater. **21**, 2463 (2009).

[13] W. I. F. David, R. M. lbberson, J. C. Matthewman, K. Prassides, T. J. S. Dennis, J. P. Hare, H. W. Kroto, R. Taylor, and D. R. M. Walton, Crystal structure and bonding of ordered C_{60}, Nature **353**, 147 (1991).

[14] S. Pekker, É. Kováts, G. Oszlányi, G. Bényei, G. Klupp, G. Bortel, I. Jalsovszky, E. Jakab, F. Borondics, K. Kamarás *et al.*, Rotor–stator molecular crystals of fullerenes with cubane, Nat. Mater. **4**, 764 (2005).

[15] For a review, see J. Harada, Plastic/ferroelectric molecular crystals: Ferroelectric performance in bulk polycrystalline forms, APL Mater. **9**, 020901 (2021).

[16] J. Harada, T. Shimojo, H. Oyamaguchi, H. Hasegawa, Y. Takahashi, K. Satomi, Y. Suzuki, J. Kawamata, and T. Inabe, Directionally tunable and mechanically deformable ferroelectric crystals from rotating polar globular ionic molecules, Nat. Chem. **8**, 946 (2016).

[17] Y.-Y. Tang, P.-F. Li, P.-P. Shi, W.-Y. Zhang, Z.-X. Wang, Y.-M. You, H.-Y. Ye, T. Nakamura, and R.-G. Xiong, Visualization of Room-Temperature Ferroelectricity and Polarization Rotation in the Thin Film of Quinuclidinium Perrhenate, Phys. Rev. Lett. **119**, 207602 (2017).

[18] Y.-M. You, Y.-Y. Tang, P.-F. Li, H.-Y. Zhang, W.-Y. Zhang, Y. Zhang, H.-Y. Ye, T. Nakamura, and R. G. Xiong, Quinuclidinium salt ferroelectric thin-film with duodecuple-rotational polarization-directions, Nat. Commun. **8**, 14934 (2017).

[19] J. Harada, N. Yoneyama, S. Yokokura, Y. Takahashi, A. Miura, N. Kitamura, and T. Inabe, Ferroelectricity and piezoelectricity in free-standing polycrystalline films of plastic crystals, J. Am. Chem. Soc. **140**, 346 (2018).

[20] Y.-Y. Tang, P.-F. Li, W.-Q. Liao, P.-P. Shi, Y.-M. You, and R.-G. Xiong, Multiaxial molecular ferroelectric thin films bring light to practical applications, J. Am. Chem. Soc. **140**, 8051 (2018).

[21] J. Harada, Y. Kawamura, Y. Takahashi, Y. Uemura, T. Hasegawa, H. Taniguchi, and K. Maruyama, Plastic/ferroelectric crystals with easily switchable polarization: Low-voltage operation, unprecedentedly high pyroelectric performance, and large piezoelectric effect in polycrystalline forms, J. Am. Chem. Soc. **141**, 9349 (2019).

[22] D. Damjanovic, Ferroelectric, dielectric and piezoelectric properties of ferroelectric thin films and ceramics, Rep. Prog. Phys. **61**, 1267 (1998).

[23] G. Catalan, J. Seidel, R. Ramesh, and J. F. Scott, Domain wall nanoelectronics, Rev. Mod. Phys. **84**, 119 (2012).

[24] Y. Uemura, S. Matsuoka, J. Tsutsumi, S. Horiuchi, S. Arai, and T. Hasegawa, Birefringent Field-Modulation Imaging of Transparent Ferroelectrics, Phys. Rev. Appl. **14**, 024060 (2020).

[25] A. Gruverman and S. V. Kalinin, Piezoresponse force microscopy and recent advances in nanoscale studies of ferroelectrics, J. Mater. Sci. **41**, 107 (2006).

[26] E. Soergel, Piezoresponse force microscopy (PFM), J. Phys. D Appl. Phys. **44**, 464003 (2011).

[27] See Supplemental Material at http://link.aps.org/supplemental/10.1103/PhysRevMaterials.7.035601 for (1) micrographs and XRD images of single-crystalline [AH][ReO_4] thin films, (2) estimation of birefringence in [AH][ReO_4] by transmittance spectra, (3) birefringent FFMI measurement of [AH][ReO_4] thin films, (4) surface topography of [AH][ReO_4] films, (5) analysis of birefringent FFMI signal at domain walls, and (6) PFM analysis for type-B and C [AH][ReO_4] films.

[28] S. K. Streiffer and C. B. Parker, Domain patterns in epitaxial rhombohedral ferroelectric films. I. Geometry and experiments, J. Appl. Phys. **83**, 2742 (1998).

[29] T. Mitsui and J. Furuichi, Domain structure of Rochelle salt and KH_2PO_4, Phys. Rev. **90**, 193 (1953).

[30] A. K. Tagantsev, L. E. Cross, and J. Fousek, *Domains in Ferroic Crystals and Thin Films* (Springer, New York, 2010).

[31] A. Schilling, T. B. Adams, R. M. Bowman, J. M. Gregg, G. Catalan, and J. F. Scott, Scaling of domain periodicity with thickness measured in BaTi O3 single crystal lamellae and comparison with other ferroics, Phys. Rev. B **74**, 024115 (2006).

[32] G. Catalan, J. F. Scott, A. Schilling, and J. M. Gregg, Wall thickness dependence of the scaling law for ferroic stripe domains, J. Phys. Condens. Matter. **19**, 022201 (2007).

[33] G. Catalan, I. Lukyanchuk, A. Schilling, J. M. Gregg, and J. F. Scott, Effect of wall thickness on the ferroelastic domain size of $BaTiO_3$, J. Mater. Sci. **44**, 5307 (2009).

[34] Y. Wu, Y. Matsushita, and Y. Suzuki, Nanoscale magnetic-domain structure in colossal magnetoresistance islands, Phys. Rev. B **64**, 220404 (2001).

[35] S. K. Streiffer, J. A. Eastman, D. D. Fong, C. Thompson, A. Munkholm, M. V. Ramana Murty, O. Auciello, G. R. Bai, and G. B. Stephenson, Observation of Nanoscale 180° Stripe Domains in Ferroelectric $PbTiO_3$ Thin Films, Phys. Rev. Lett. **89**, 067601 (2002).

[36] P. D. Sparks, N. P. Stern, D. S. Snowden, B. A. Kappus, J. G. Checkelsky, S. S. Harberger, A. M. Fusello, and J. C. Eckert, Stripe domains and magnetoresistance in thermally deposited nickel films, J. Magn. Magn. Mater. **272**, E1339 (2004).

[37] F. Dumas-Bouchiat, H. S. Nagaraja, F. Rossignol, C. Champeaux, and A. Catherinot, Magnetic domains in Co-cluster assembled films deposited by LECBD, Appl. Surf. Sci. **247**, 76 (2005).

[38] P. Sharma, T. Reece, D. Wu, V. M. Fridkin, S. Ducharme, and A. Gruverman, Nanoscale domain patterns in ultrathin polymer ferroelectric films, J. Phys. Condens. Matter. **21**, 485902 (2009).

[39] V. Shelke, D. Mazumdar, S. Jesse, S. Kalinin, A. Baddorf, and A. Gupta, Ferroelectric domain scaling and switching in ultrathin $BiFeO_3$ films deposited on vicinal substrates, New J. Phys. **14**, 053040 (2012).

[40] Y. Ahn, J. Seo, J. Yeog Son, and J. Jang, Ferroelectric domain structures and thickness scaling of epitaxial $BiFeO_3$ thin films, Mater. Lett. **154**, 25 (2015).

[41] Y. Ahn, J. Seo, K. J. Lee, and J. Y. Son, Ferroelectric domain of epitaxial $AgNbO_3$ thin film, J. Cryst. Growth. **437**, 10 (2016).